

Topological Charges, Fermi Arcs, and Surface States of K_4 Crystal

Shoya Yoshida,¹ Katsuhiro Takahashi,¹ and Katsunori Wakabayashi^{1,2,3}

¹*Department of Nanotechnology for Sustainable Energy, School of Science and Technology, Kwansei Gakuin University, Gakuen-Uegahara 1, Sanda, 669-1330, Japan*

²*Center for Spintronics Research Network (CSRN), Osaka University, Toyonaka 560-8531, Japan*

³*National Institute for Materials Science (NIMS), Namiki 1-1, Tsukuba 305-0044, Japan*

(Dated: January 21, 2026)

We investigate the topological electronic properties of the K_4 crystal by constructing a tight-binding model. The bulk band structure hosts Weyl nodes with higher and conventional chiralities ($\chi = \pm 2$ and $\chi = \pm 1$) located at high-symmetry points in the Brillouin zone. Through analytical evaluation of the Berry curvature, we identify the positions and chiralities of these Weyl nodes. Furthermore, slab calculations for the (001) surface reveal Fermi arcs that connect Weyl nodes of opposite chirality, including those linking $\chi = \pm 2$ nodes with pairs of $\chi = \mp 1$ nodes. These results demonstrate that the K_4 crystal is a spinless Weyl semimetal featuring topologically protected surface states originating from multiple types of Weyl nodes.

I. INTRODUCTION

In recent years, the study of topological materials—including topological insulators [1–12], topological crystalline insulators [13, 14], topological magnets [15, 16], and Dirac and Weyl semimetals [17, 18]—has revealed novel quantum phases characterized by topological invariants and robust surface states [5, 19]. Among these systems, Weyl semimetals are distinguished by pairs of topologically protected band crossings, known as Weyl nodes, which act as monopoles of Berry curvature in momentum space [17, 20]. A hallmark feature of Weyl semimetals is the emergence of open surface states, called Fermi arcs, which connect projections of Weyl nodes with opposite chirality in the slab Brillouin zone [18]. These arcs directly reflect the nontrivial bulk topology and serve as unambiguous experimental signatures of Weyl physics [18, 21]. Understanding how Fermi arcs emerge and how their connectivity is dictated by the underlying crystal symmetry has become a central theme in the exploration of topological materials.

The theoretical design of novel crystal structures, inspired by mathematical principles not realized in nature, has attracted considerable attention in recent years. One prominent example is the K_4 lattice, a mathematical construct defined as the maximal abelian covering graph of the complete graph K_4 [22, 23]. Owing to its unique geometry, this structure has been referred to by various alternative names, including the diamond twin [24], the srs lattice [23, 25, 26], and the Laves graph [23, 27]. It is also closely related to the Gyroid surface [23, 27], a chiral network found in nature for instance, in butterfly wing scales [28]. Although the K_4 lattice has not yet been directly observed in natural systems, the existence of structurally analogous biological networks suggests that such mathematical constructs can serve as blueprints for the design of novel materials in both synthetic and biological contexts.

In condensed matter physics, the K_4 crystal has attracted considerable interest because its unique topology and electronic structure are expected to give rise to unprecedented physical properties [29–31]. Materials adopting this crystal are predicted to exhibit electronic behaviors distinct from those of familiar carbon allotropes such as graphene [32–34]

and diamond [35, 36]. This highlights the potential of the K_4 crystal as a guiding principle for the design of functional materials in both solid crystals and self-assembled architectures. Theoretical investigations of the K_4 crystal have extended beyond carbon allotropes to a wide range of other material systems. For example, boron and phosphorus K_4 crystals can form stable sp^2 chiral structures [37, 38]. Moreover, multi-element K_4 crystals have been proposed through doping or intercalation, including hydrogenated K_4 carbon [39], carbon-doped K_4 nitrogen [40], and K_4 -like NaC_2 [41]. The K_4 crystal structure has been experimentally realized via electrochemical crystallization of radical anion salts derived from a triangular molecule [42].

One of the most striking features of the K_4 crystal is the emergence of a so-called *triple Dirac cone* in its electronic band structure. At high-symmetry points such as Γ and H , two linearly dispersing bands intersect with an almost flat band, forming a pseudospin-1 Dirac point [30]. Such band crossings are rare in crystalline systems.

Beyond conventional Dirac and Weyl fermions, the discovery of multi-fold band degeneracies has opened new directions in the study of topological phases. Crystalline symmetries can stabilize higher-fold fermions such as triple-point fermions, spin-1 Weyl fermions, and other exotic quasiparticles, which in turn host unconventional topological charges and novel transport or surface phenomena [43–51]. These studies highlight that the triple Dirac cone in the K_4 crystal belongs to a broader framework of topological semimetals stabilized by symmetry-protected degeneracies.

In this work, we construct a tight-binding model of the K_4 crystal using one s orbital per site with nearest-neighbor hopping and analyze the resulting band structure. By evaluating the Berry curvature [52–61], we identify Weyl nodes at high-symmetry points including Γ , H , and P , and classify them according to their chirality. We further investigate the surface states in a (001) slab geometry, demonstrating the presence of topological Fermi arcs that connect Weyl nodes of different chiralities. In particular, we show that higher-chirality ($\chi = \pm 2$) Weyl nodes are linked to pairs of conventional ($\chi = \pm 1$) nodes via topologically protected surface states.

Thus, this study fills a crucial knowledge gap: demonstrating that the K_4 crystal is not only a mathematically in-

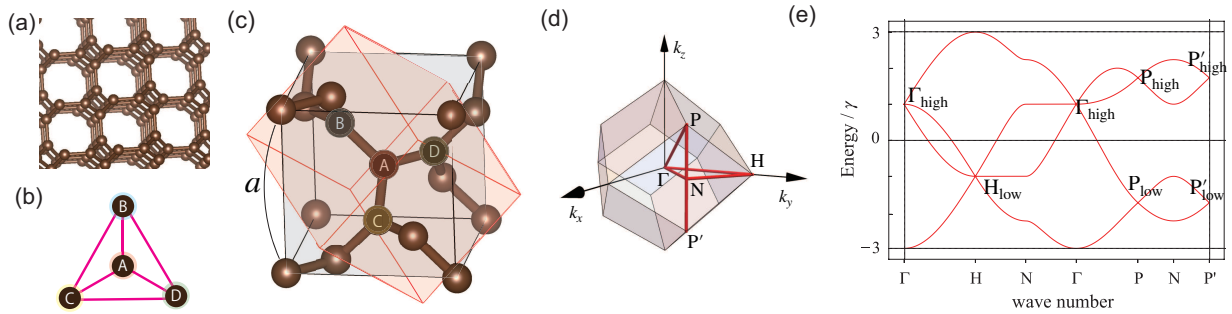


FIG. 1. (a) Crystal structure of the K_4 crystal. Viewed along the (001) direction, it exhibits a pattern of tiled squares and octagons and contains multiple helical motifs. (b) Graph representation of the K_4 structure, showing the connectivity of the four sublattices. The corresponding graph is a complete graph with four vertices, each connected to all others by three edges. (c) Unit cell of the K_4 crystal. The gray cube represents the conventional cubic unit cell, while the red rhombohedron denotes the primitive unit cell of the body-centered cubic (bcc) lattice. The primitive cell contains four sublattices, labeled A-D, each connected by three nearest-neighbor bonds. At each site, three bonds extend isotropically in a single plane, similar to graphene. However, the bond plane at one site is rotated by an angle of $\theta \simeq 70.5^\circ$ ($\cos \theta = 1/3$) relative to that of a neighboring site. (d) First Brillouin zone (BZ) of the K_4 crystal, based on the bcc lattice. (e) Energy band structure of the K_4 crystal. At the Γ point, two linearly dispersing (conical) bands and one flat band intersect at energy γ , referred to as the Γ_{high} point. At the H point, a similar crossing occurs at energy $-\gamma$, labeled as the H_{low} point. The four-band structure around H_{low} is the vertical inversion of that around Γ_{high} . At the P points, two conical bands form vertically aligned degenerate points at energies $-\sqrt{3}\gamma$ and $+\sqrt{3}\gamma$, denoted as P_{low} and P'_{high} , respectively.

triguing lattice construct or a metallic carbon allotrope, but also a bona fide Weyl semimetal with topologically nontrivial surface states. This establishes the K_4 crystal as a novel archetype of three-dimensional sp^2 -hybridized carbon with intrinsic topological properties.

II. CRYSTAL AND BAND STRUCTURE

Figure 1(a) shows the crystal structure of the K_4 crystal. It can be regarded as a three-dimensional realization of the complete graph K_4 , in which all four vertices are mutually connected. This unique connectivity is reflected in the atomic arrangement shown in Fig. 1(b), where each site forms bonds with the other three. As a result, three bonds emanate from each site in a coplanar configuration; however, the planes formed by these bonds are twisted relative to those of neighboring sites by an angle $\theta \simeq 70.5^\circ$ (with $\cos \theta = 1/3$). When all such planes are aligned parallel, the resulting structure reduces to the two-dimensional honeycomb lattice. Thus, the K_4 crystal can be viewed as a three-dimensional extension of the honeycomb structure.

The crystal structure of K_4 is derived from this connectivity of K_4 graph. It adopts a body-centered cubic (bcc) lattice with space group $I4_132$, which lacks inversion symmetry and thus renders the system noncentrosymmetric. The conventional unit cell with lattice constant a is shown in Fig. 1(c). The rhombohedral primitive cell denoted by the red rhombohedron in Fig. 1(c) is spanned by the translation vectors

$$\mathbf{a}_1 = \frac{a}{2}(-1, 1, 1), \mathbf{a}_2 = \frac{a}{2}(1, -1, 1), \mathbf{a}_3 = \frac{a}{2}(1, 1, -1),$$

and contains four atomic sites labeled A , B , C , and D . The fractional coordinates of the four sublattice sites are given by

$$\mathbf{R}_A = a(0, 0, 0), \quad \mathbf{R}_B = a\left(\frac{1}{2}, \frac{1}{4}, -\frac{1}{4}\right),$$

$$\mathbf{R}_C = a\left(-\frac{1}{4}, \frac{1}{2}, \frac{1}{4}\right), \quad \mathbf{R}_D = a\left(\frac{1}{4}, -\frac{1}{4}, \frac{1}{2}\right).$$

Each site is connected to its three nearest neighbors by the displacement vectors τ_{ij} ($i, j = A, B, C, D$), among which six are independent:

$$\begin{aligned} \tau_{AB} &= \frac{a}{4}(0, 1, -1), \tau_{AC} = \frac{a}{4}(-1, 0, 1), \tau_{AD} = \frac{a}{4}(1, -1, 0), \\ \tau_{BC} &= \frac{a}{4}(1, 1, 0), \tau_{BD} = \frac{a}{4}(-1, 0, -1), \tau_{CD} = \frac{a}{4}(0, 1, 1). \end{aligned}$$

The corresponding reciprocal vectors are given as

$$\mathbf{b}_1 = \frac{2\pi}{a}(0, 1, 1), \mathbf{b}_2 = \frac{2\pi}{a}(1, 0, 1), \mathbf{b}_3 = \frac{2\pi}{a}(1, 1, 0).$$

Thus, the first Brillouin zone (BZ) of the bcc lattice has a rhombohedral shape, as shown in Fig. 1(d), with the following representative high-symmetry points:

$$\begin{aligned} \Gamma &: (0, 0, 0), & H &: \left(0, \frac{2\pi}{a}, 0\right), \\ N &: \left(\frac{\pi}{a}, \frac{\pi}{a}, 0\right), & P &: \left(\frac{\pi}{a}, \frac{\pi}{a}, \frac{\pi}{a}\right), P' &: \left(\frac{\pi}{a}, \frac{\pi}{a}, -\frac{\pi}{a}\right). \end{aligned}$$

The symmetry properties of the high-symmetry points (k -point little groups) in the Brillouin zone are summarized as follows. The Γ and H points belong to the O point group (432). The Γ point is unique under this symmetry, while the H point has six symmetry-equivalent points located at $(\pm \frac{2\pi}{a}, 0, 0)$, $(0, \pm \frac{2\pi}{a}, 0)$, and $(0, 0, \pm \frac{2\pi}{a})$. The P and P' points belong to the T point group (23). Each of these has four symmetry-equivalent points related by the cubic symmetry operations:

$$\begin{aligned} \mathbf{P} : & \left(+\frac{\pi}{a}, +\frac{\pi}{a}, +\frac{\pi}{a} \right), \left(+\frac{\pi}{a}, -\frac{\pi}{a}, -\frac{\pi}{a} \right), \left(-\frac{\pi}{a}, +\frac{\pi}{a}, -\frac{\pi}{a} \right), \left(-\frac{\pi}{a}, -\frac{\pi}{a}, +\frac{\pi}{a} \right), \\ \mathbf{P}' : & \left(-\frac{\pi}{a}, -\frac{\pi}{a}, -\frac{\pi}{a} \right), \left(-\frac{\pi}{a}, +\frac{\pi}{a}, +\frac{\pi}{a} \right), \left(+\frac{\pi}{a}, -\frac{\pi}{a}, +\frac{\pi}{a} \right), \left(+\frac{\pi}{a}, +\frac{\pi}{a}, -\frac{\pi}{a} \right). \end{aligned}$$

The N point is invariant only under the identity operation, and no band degeneracy occurs there, so we omit a detailed discussion.

We construct a tight-binding model for K_4 crystal by assuming a single s -orbital per site and only nearest-neighbor hopping. The onsite energy is set to zero at all sites. Thus, the eigenvalue equation of K_4 crystal reads

$$\hat{H}(\mathbf{k})|u_j(\mathbf{k})\rangle = E_j(\mathbf{k})|u_j(\mathbf{k})\rangle,$$

where $\mathbf{k} = (k_x, k_y, k_z)$ is the wavenumber vector and $j (= 1, 2, 3, 4)$ is the band index. The eigenvector is defined as $|u_j(\mathbf{k})\rangle = (\psi_{jA}(\mathbf{k}), \psi_{jB}(\mathbf{k}), \psi_{jC}(\mathbf{k}), \psi_{jD}(\mathbf{k}))^T$, where $(\cdots)^T$ indicates the transpose of the vector. $\psi_{j\alpha}(\mathbf{k})$ ($\alpha = A, B, C, D$)

is the amplitude at site α for j -th energy band at \mathbf{k} . The Hamiltonian in momentum space takes the form of a 4×4 Hermitian matrix $H(\mathbf{k})$, where each matrix element represents hopping between two sites connected by a nearest-neighbor bond. The off-diagonal matrix element, $h_{ij}(\mathbf{k})$, which means the electron hopping from site j to site i , is given by

$$h_{ij}(\mathbf{k}) = -\gamma e^{-i\mathbf{k} \cdot \tau_{ij}},$$

where $i, j = 1, 2, 3, 4$. γ is the nearest-neighbor hopping amplitude. τ_{ij} is the displacement vector from site j to site i . Since we have assumed the onsite potential is set to zero at all sites, the diagonal matrix elements are zero, i.e., $h_{ii}(\mathbf{k}) = 0$. Thus the resulting Hamiltonian matrix is explicitly written as

$$\hat{H}(\mathbf{k}) = -\gamma \begin{pmatrix} 0 & e^{-i(k_y-k_z)\frac{a}{4}} & e^{-i(k_z-k_x)\frac{a}{4}} & e^{-i(k_x-k_y)\frac{a}{4}} \\ e^{i(k_y-k_z)\frac{a}{4}} & 0 & e^{-i(k_x+k_y)\frac{a}{4}} & e^{-i(-k_z-k_x)\frac{a}{4}} \\ e^{i(k_z-k_x)\frac{a}{4}} & e^{i(k_x+k_y)\frac{a}{4}} & 0 & e^{-i(k_y+k_z)\frac{a}{4}} \\ e^{i(k_x-k_y)\frac{a}{4}} & e^{i(-k_z-k_x)\frac{a}{4}} & e^{i(k_y+k_z)\frac{a}{4}} & 0 \end{pmatrix}. \quad (1)$$

Figure 1(e) shows the band structure of the K_4 crystal obtained from this tight-binding model. At the band degeneracy points Γ_{high} and H_{low} , we find a threefold band crossing composed of two linearly dispersing bands forming a Dirac cone, together with a nearly flat band intersecting at the same point. This type of threefold degeneracy is termed a *triple Dirac cone*. In contrast, at the P_{low} and P_{high} points, a twofold degeneracy forms a conventional Dirac cone with linear dispersion.

From the viewpoint of group theory, the 3+1 band degeneracy structure at the Γ and H points is classified as the di-

rect sum of irreducible representations $T_2 \oplus A_1$ of the O point group. Likewise, the 2+2 degeneracy at the P and P' points corresponds to the $E \oplus E$ representation of the T point group.

Furthermore, the band degeneracies can be understood from the viewpoint of Wyckoff positions [62, 63] and elementary band representations (EBRs) [64]. The four sublattices in the K_4 unit cell occupy the Wyckoff position $8a$ of the space group $I4_132$ (No. 214), whose site symmetry is 32 (the D_3 point group). Table I summarizes the band representations induced from the $8a$ Wyckoff position, taken from the Bilbao Crystallographic Server [65].

TABLE I. Band representations for the Wyckoff position $8a$ ($1/8, 1/8, 1/8$) of space group $I4_132$ (No. 214)

Band-Rep.	$A_1 \uparrow G(4)$	$A_2 \uparrow G(4)$	$E \uparrow G(8)$
$\Gamma : (0, 0, 0)$	$\Gamma_1(1) \oplus \Gamma_5(3)$	$\Gamma_2(1) \oplus \Gamma_4(3)$	$\Gamma_3(2) \oplus \Gamma_4(3) \oplus \Gamma_5(3)$
$\text{H} : (1, 1, 1)$	$H_2(1) \oplus H_4(3)$	$H_1(1) \oplus H_5(3)$	$H_3(2) \oplus H_4(3) \oplus H_5(3)$
$\text{P} : (1/2, 1/2, 1/2)$	$P_1(2) \oplus P_3(2)$	$P_1(2) \oplus P_3(2)$	$P_1(2) \oplus 2P_2(2) \oplus P_3(2)$
$\text{N} : (1/2, 1/2, 0)$	$2N_1(1) \oplus N_3(1) \oplus N_4(1)$	$2N_2(1) \oplus N_3(1) \oplus N_4(1)$	$2N_1(1) \oplus 2N_2(1) \oplus 2N_3(1) \oplus 2N_4(1)$

For the spinless s -orbital tight-binding model, the bands

transform according to the elementary band representation

$A_1 \uparrow G(4)$. Consequently, at the Γ and H points, this representation decomposes into $\Gamma_1 \oplus \Gamma_5$ and $H_2 \oplus H_4$, respectively, producing the characteristic $3+1$ band degeneracy. At the P point, it yields $P_1 \oplus P_3$, leading to the observed $2+2$ degeneracy. Since the calculated bands coincide with a sum of elementary band representations (EBRs), the system is classified as being in an atomic limit.

When the p_x , p_y , and p_z orbitals are included, the atomic degrees of freedom generate the representation

$$A_1 \uparrow G(4) \oplus A_2 \uparrow G(4) \oplus E \uparrow G(8).$$

Here, $A_2 \uparrow G(4)$ corresponds to the p orbital perpendicular to the coplanar plane spanned by the three nearest-neighbor bonds, and $E \uparrow G(8)$ corresponds to the remaining two in-plane p orbitals. The hybridization of s and p orbitals form the π bands, in which triple degeneracies at Γ and H and the double degeneracies at P persist in the same manner as in the s -orbital model.

Thus, these degeneracies persist even in the multiorbital ($s+p$) system, as confirmed by symmetry analysis. In addition, the same degeneracies have been reported in first-principles calculations [29, 30]. This indicates that the minimal s -orbital model already captures the essential topological features of the K_4 crystal.

III. TOPOLOGICAL CHARGE

In this section, we demonstrate that the band degeneracies identified in K_4 crystal correspond to Weyl points, each carrying a quantized topological charge (chirality).

A. Weyl points

A Weyl point is a singularity in momentum space at which two or more energy bands cross linearly in all directions, giving

rise to gapless excitations governed by the Weyl equation [17, 20, 66]. Near such a point \mathbf{k}_0 , the effective Hamiltonian can be expressed as

$$H(\mathbf{q}) = (E_0 + \mathbf{v}_0 \cdot \mathbf{q})I + \sum_{i=x,y,z} \mathbf{v}_i \cdot \mathbf{q} \sigma_i, \quad (2)$$

where $\mathbf{q} = \mathbf{k} - \mathbf{k}_0$ is the wavevector measured from the Weyl point, E_0 and \mathbf{v}_0 denote the energy and group velocity at \mathbf{k}_0 , I is the identity matrix, σ_i are the Pauli matrices, and \mathbf{v}_i represent the effective velocities along the i -axis.

Here, we explicitly construct the effective Hamiltonians around the degeneracy points Γ_{high} , H_{low} , P_{low} and P_{high} , in the K_4 crystal and calculate eigenvalues and eigenfunctions. The effective Hamiltonians are obtained by expanding the tight-binding Hamiltonian [Eq. (1)] to first order in \mathbf{k} and applying appropriate unitary transformations that diagonalize the zeroth-order Hamiltonians at each Weyl point. For related methods and eigenvalue analyses, see Ref. [30].

We first focus on the triple band degeneracy located at the Γ_{high} point, which consists of two dispersive (conical) bands and one flat band. At the Γ point ($\mathbf{k} = (0, 0, 0)$), the zeroth-order Hamiltonian is given by

$$H_{\Gamma}^{(0)} = -\gamma \begin{pmatrix} 0 & 1 & 1 & 1 \\ 1 & 0 & 1 & 1 \\ 1 & 1 & 0 & 1 \\ 1 & 1 & 1 & 0 \end{pmatrix},$$

where the Bloch phase factors drop out, and the four tight-binding basis states $|A\rangle$, $|B\rangle$, $|C\rangle$, and $|D\rangle$ are connected by equivalent hopping $-\gamma$. This connectivity corresponds to the K_4 graph (Fig. 1(b)) itself and can be viewed as a regular tetrahedron. The representation of these four basis functions follows the point group T_d , which decomposes into the irreducible representations A_1 and T_2 , giving rise to one nondegenerate state (A_1 , $E = -3\gamma$) and one triply degenerate state (T_2 , $E = +\gamma$) at the Γ point.

Expanding the Hamiltonian to first order in \mathbf{k} , we obtain

$$H_{\Gamma}^{(1)}(\mathbf{k}) = -\gamma \begin{pmatrix} 0 & 1 & 1 & 1 \\ 1 & 0 & 1 & 1 \\ 1 & 1 & 0 & 1 \\ 1 & 1 & 1 & 0 \end{pmatrix} - \frac{\gamma a}{4} \begin{pmatrix} 0 & -i(k_y - k_z) & -i(k_z - k_x) & -i(k_x - k_y) \\ i(k_y - k_z) & 0 & -i(k_x + k_y) & -i(-k_z - k_x) \\ i(k_z - k_x) & i(k_x + k_y) & 0 & -i(k_y + k_z) \\ i(k_x - k_y) & i(-k_z - k_x) & i(k_y + k_z) & 0 \end{pmatrix}.$$

This Hamiltonian can be block-diagonalized using the unitary transformation U_{Γ} :

$$U_{\Gamma}^{\dagger} H_{\Gamma}^{(1)}(\mathbf{k}) U_{\Gamma} = -\gamma \begin{pmatrix} 3 & 0 & 0 & 0 \\ 0 & -1 & 0 & 0 \\ 0 & 0 & -1 & 0 \\ 0 & 0 & 0 & -1 \end{pmatrix} - \frac{\gamma a}{2} \begin{pmatrix} 0 & 0 & 0 & 0 \\ 0 & k_z & \frac{1}{\sqrt{2}}k_- & 0 \\ 0 & \frac{1}{\sqrt{2}}k_+ & 0 & \frac{1}{\sqrt{2}}k_- \\ 0 & 0 & \frac{1}{\sqrt{2}}k_+ & -k_z \end{pmatrix},$$

where $k = \sqrt{k_x^2 + k_y^2 + k_z^2}$ and $k_{\pm} = k_x \pm ik_y$.

The unitary matrix U_Γ is constructed from the zeroth-order eigenfunctions at the Γ point as

$$U_\Gamma = \frac{1}{2} \begin{pmatrix} 1 & e^{-i\frac{\pi}{4}} & e^{+i\frac{\pi}{2}} & e^{+i\frac{3\pi}{4}} \\ 1 & e^{-i\frac{3\pi}{4}} & e^{-i\frac{\pi}{2}} & e^{+i\frac{\pi}{4}} \\ 1 & e^{+i\frac{\pi}{4}} & e^{-i\frac{\pi}{2}} & e^{-i\frac{3\pi}{4}} \\ 1 & e^{+i\frac{3\pi}{4}} & e^{+i\frac{\pi}{2}} & e^{-i\frac{\pi}{4}} \end{pmatrix},$$

where the eigenvector $(1, 1, 1, 1)^T$ corresponds to the A_1 representation ($E = -3\gamma$), while the other three orthogonal eigenvectors correspond to the triply degenerate T_2 representation ($E = +\gamma$).

By discarding the lowest-energy flat band ($E = -3\gamma$), we

obtain the following effective three-band Hamiltonian around the Γ_{high} point:

$$H_{\Gamma_{\text{high}},\text{eff}}(\mathbf{k}) = -\frac{\gamma a}{2} \begin{pmatrix} k_z & \frac{1}{\sqrt{2}}k_- & 0 \\ \frac{1}{\sqrt{2}}k_+ & 0 & \frac{1}{\sqrt{2}}k_- \\ 0 & \frac{1}{\sqrt{2}}k_+ & -k_z \end{pmatrix}.$$

This can be written compactly as

$$H_{\Gamma_{\text{high}},\text{eff}}(\mathbf{k}) = -\frac{\gamma a}{2} \mathbf{k} \cdot \mathbf{S} \quad (3)$$

where $\mathbf{S} = (S_x, S_y, S_z)$ denotes the spin-1 matrices:

$$\mathbf{S} = (S_x, S_y, S_z) = \left(\begin{pmatrix} 0 & \frac{1}{\sqrt{2}} & 0 \\ \frac{1}{\sqrt{2}} & 0 & \frac{1}{\sqrt{2}} \\ 0 & \frac{1}{\sqrt{2}} & 0 \end{pmatrix}, \begin{pmatrix} 0 & -\frac{i}{\sqrt{2}} & 0 \\ +\frac{i}{\sqrt{2}} & 0 & -\frac{i}{\sqrt{2}} \\ 1 & +\frac{i}{\sqrt{2}} & 0 \end{pmatrix}, \begin{pmatrix} 1 & 0 & 0 \\ 0 & 0 & 0 \\ 0 & 0 & -1 \end{pmatrix} \right).$$

The corresponding eigenvalues are

$$E_{\Gamma_{\text{high}}}^- = -\frac{\gamma a}{2}k, \quad E_{\Gamma_{\text{high}}}^0 = 0, \quad E_{\Gamma_{\text{high}}}^+ = +\frac{\gamma a}{2}k,$$

corresponding to a lower conical band, a flat middle band, and an upper conical band, meeting at the Γ_{high} point to form a *triple Dirac cone* [Fig. 2].

The normalized eigenfunctions of the effective Hamiltonian $H_{\Gamma_{\text{high}},\text{eff}}(\mathbf{k})$ [Eq. (3)] are given by

$$\mathbf{u}_{\Gamma_{\text{high}}}^- = \frac{1}{2k(k_z + k)} \begin{pmatrix} (k_z + k)^2 \\ \sqrt{2}k_+(k_z + k) \\ k_+^2 \end{pmatrix}, \quad \mathbf{u}_{\Gamma_{\text{high}}}^0 = \frac{1}{\sqrt{2}k} \begin{pmatrix} -k_- \\ \sqrt{2}k_z \\ k_+ \end{pmatrix}, \quad \mathbf{u}_{\Gamma_{\text{high}}}^+ = \frac{1}{2k(k_z - k)} \begin{pmatrix} (k_z - k)^2 \\ \sqrt{2}k_+(k_z - k) \\ k_+^2 \end{pmatrix}.$$

The effective Hamiltonians at the H_{low} , P_{low} , and P_{high} points, which exhibit Weyl-type linear dispersions, are derived in Appendix A. Here, we summarize their explicit forms.

For the H_{low} point:

$$H_{H_{\text{low}},\text{eff}}(\mathbf{k}) = +\frac{\gamma a}{2} \begin{pmatrix} k_z & \frac{1}{\sqrt{2}}k_- & 0 \\ \frac{1}{\sqrt{2}}k_+ & 0 & \frac{1}{\sqrt{2}}k_- \\ 0 & \frac{1}{\sqrt{2}}k_+ & -k_z \end{pmatrix} = +\frac{\gamma a}{2} \mathbf{k} \cdot \mathbf{S}.$$

Note that the effective Hamiltonian at the H_{low} point has the same matrix structure as that at the Γ_{high} point, but with an overall sign reversal in front of $\mathbf{k} \cdot \mathbf{S}$.

For the P point ($\mathbf{k} = (\frac{\pi}{a}, \frac{\pi}{a}, \frac{\pi}{a})$), two inequivalent Weyl points appear, denoted as P_{low} and P_{high} , corresponding to distinct energy sectors $E = \mp\sqrt{3}\gamma$, respectively:

$$H_{P_{\text{low}},\text{eff}}(\mathbf{k}) = +\frac{\gamma a}{6} \begin{pmatrix} k_x + k_y + k_z & \sqrt{2}(\omega k_x + \omega^2 k_y + k_z) \\ \sqrt{2}(\omega^2 k_x + \omega k_y + k_z) & -k_x - k_y - k_z \end{pmatrix},$$

and

$$H_{P_{\text{high}},\text{eff}}(\mathbf{k}) = +\frac{\gamma a}{6} \begin{pmatrix} k_x + k_y + k_z & \sqrt{2}(\omega^2 k_x + \omega k_y + k_z) \\ \sqrt{2}(\omega k_x + \omega^2 k_y + k_z) & -k_x - k_y - k_z \end{pmatrix},$$

where $\omega = \frac{-1+i\sqrt{3}}{2}$, $\omega^3 = 1$. The P_{low} and P_{high} Hamiltoni-

ans represent two symmetry-inequivalent linear band cross-

ings originating from distinct doublet states in the tight-binding spectrum.

Since the effective Hamiltonian at the P' point is related to that at the P point by a unitary transformation, we restrict our discussion to the P point.

B. Berry curvature and topological charge

To evaluate the topological nature of each Weyl point, we compute the Berry connection and curvature from the corresponding eigenfunctions. Physically, the Berry connection can be regarded as a vector potential in momentum space, and the Berry curvature as its associated magnetic field in momentum space. The Berry connection $\mathbf{A}^j(\mathbf{k})$ for the j -th band is defined as

$$\mathbf{A}^j(\mathbf{k}) = (A_x^j(\mathbf{k}), A_y^j(\mathbf{k}), A_z^j(\mathbf{k})),$$

where

$$A_\alpha^j = i\langle u_j(\mathbf{k}) | \frac{\partial}{\partial k_\alpha} | u_j(\mathbf{k}) \rangle, \quad \alpha = x, y, z.$$

The Berry curvature $\Omega_j(\mathbf{k})$ for j -th band is then given as the rotation of Berry connection, i.e.,

$$\Omega_j(\mathbf{k}) = \nabla_{\mathbf{k}} \times \mathbf{A}^j(\mathbf{k}),$$

where $\nabla_{\mathbf{k}} = (\frac{\partial}{\partial k_x}, \frac{\partial}{\partial k_y}, \frac{\partial}{\partial k_z})$.

Weyl points are characterized by a topological charge ϕ [17, 67–69] and a chirality χ [17, 66], which quantify their role as monopoles of the Berry curvature in momentum space. The topological charge ϕ_j of the j -th band is defined as the Berry flux through a closed surface S enclosing the Weyl point,

$$\phi_j = \int_S \Omega_j \cdot d\mathbf{S}.$$

The chirality χ of a Weyl point is given by the total Berry flux from all occupied bands, normalized by 2π , when the Fermi level is located at the degeneracy:

$$\chi = \frac{1}{2\pi} \sum_{j=1}^{N_{\text{occ}}} \phi_j.$$

A Weyl point with $\chi > 0$ acts as a source of Berry curvature, whereas $\chi < 0$ represents a sink.

The topological charges and chiralities of the Weyl points in the K_4 crystal, which characterize their monopole nature in momentum space, are summarized in Fig. 2.

At the Γ_{high} point, the Berry connections $\mathbf{A}_{\Gamma_{\text{high}}}$ are ob-

tained from the corresponding eigenfunctions $\mathbf{u}_{\Gamma_{\text{high}}}$ as

$$\mathbf{A}_{\Gamma_{\text{high}}}^- = \frac{1}{k(k_z + k)} \begin{pmatrix} k_y \\ -k_x \\ 0 \end{pmatrix},$$

$$\mathbf{A}_{\Gamma_{\text{high}}}^0 = \mathbf{0},$$

$$\mathbf{A}_{\Gamma_{\text{high}}}^+ = \frac{1}{k(k_z - k)} \begin{pmatrix} -k_y \\ k_x \\ 0 \end{pmatrix}.$$

The corresponding Berry curvatures are given by

$$\Omega_{\Gamma_{\text{high}}}^- = -\frac{\mathbf{k}}{k^3}, \quad \Omega_{\Gamma_{\text{high}}}^0 = \mathbf{0}, \quad \Omega_{\Gamma_{\text{high}}}^+ = +\frac{\mathbf{k}}{k^3}.$$

Thus, at the Γ_{high} , the Berry curvature exhibits a monopole-like distribution, isotropic in momentum space and decaying as $1/k^2$ away from the degeneracy point.

At Γ_{high} , the topological charges are higher in magnitude and remain quantized regardless of the choice of the enclosed surface S :

$$\phi_{\Gamma_{\text{high}}}^- = -4\pi, \quad \phi_{\Gamma_{\text{high}}}^0 = 0, \quad \phi_{\Gamma_{\text{high}}}^+ = +4\pi.$$

The charge of the lower (upper) conical band is a higher topological charge (twice that of a conventional Weyl point), acting as a sink (source) of Berry curvature, while the crossing flat band carries zero charge.

The isolated band ($E = -3\gamma$) is topologically trivial, since its Berry curvature and connection both vanish. Therefore, the total chirality at Γ_{high} is $\chi = -2$, given by the sum of $\phi_{\Gamma_{\text{high}}}^-$ and $\phi_{\Gamma_{\text{high}}}^+$ divided by 2π .

Topological properties of other degeneracy points, H_{low} , P_{low} , and P_{high} are analytically derived in Appendix A.

For the H_{low} point, the Berry curvatures are

$$\Omega_{H_{\text{low}}}^- = +\frac{\mathbf{k}}{k^3}, \quad \Omega_{H_{\text{low}}}^0 = \mathbf{0}, \quad \Omega_{H_{\text{low}}}^+ = -\frac{\mathbf{k}}{k^3}.$$

This has the same form as that at Γ_{high} , but with opposite sign. Consequently, the H_{low} point possesses a total chirality of $\chi = +2$, indicating that it is a Weyl node with higher topological charge, opposite in sign to Γ_{high} .

For the P_{low} and P_{high} points, the Berry curvatures are obtained as

$$\Omega_{P_{\text{low}}}^- = \frac{-\mathbf{k}}{2k^3}, \quad \Omega_{P_{\text{low}}}^+ = \frac{+\mathbf{k}}{2k^3},$$

and

$$\Omega_{P_{\text{high}}}^- = \frac{+\mathbf{k}}{2k^3}, \quad \Omega_{P_{\text{high}}}^+ = \frac{-\mathbf{k}}{2k^3}.$$

The signs of the upper and lower bands, as well as those of P_{low} and P_{high} , are reversed.

These Berry curvatures have half the amplitude compared to those at Γ_{high} and H_{low} , indicating that P_{low} and P_{high} correspond to conventional Weyl points.

Thus, at all Weyl points in the K_4 crystal (Γ_{high} , H_{low} , P_{low} , and P_{high}), the Berry curvature exhibits a monopole-like distribution. According to the Nielsen-Ninomiya theorem [20, 70, 71], the total chirality over the entire Brillouin zone (BZ) must vanish. Therefore, Weyl points always appear in pairs or sets whose chiralities sum to zero. In the K_4 crystal, this condition is satisfied, as the BZ contains one symmetry-equivalent Γ (or H) point and two symmetry-equivalent P points, whose total chirality exactly cancels to zero.

In systems preserving time-reversal symmetry but lacking inversion symmetry, Weyl points with the same chirality must occur at momenta \mathbf{k} and $-\mathbf{k}$, since

$$\Omega(\mathbf{k}) = -\Omega(-\mathbf{k}) \Rightarrow \chi(\mathbf{k}) = \chi(-\mathbf{k}).$$

A distinctive feature of the K_4 crystal is the existence of a Weyl point at Γ_{high} that lacks a counterpart at the opposite momentum. In systems with time-reversal symmetry but without inversion symmetry, Weyl points must appear in pairs with the same chirality at \mathbf{k} and $-\mathbf{k}$, owing to the relation

$$\Omega(\mathbf{k}) = -\Omega(-\mathbf{k}) \Rightarrow \chi(\mathbf{k}) = \chi(-\mathbf{k}).$$

In the K_4 crystal, the H and P points satisfy this condition due to their positions on the Brillouin zone (BZ) boundary, as they are mapped onto themselves or symmetry-equivalent points under momentum inversion. In contrast, the Γ point lies at the BZ center and effectively pairs with itself.

Because the Weyl points appear at different energies, tuning the Fermi level near a single Weyl point allows the system to exhibit its associated topological effects independently—such as chiral-anomaly-induced transport or asymmetric surface states—without interference from other Weyl nodes.

It is also worth noting that recent works have explored the role of crystal symmetry - especially screw and rotational symmetries - in realizing Weyl nodes with higher chiral charges (for example, Ref. [72], and Ref. [73]). While such symmetry-enforced, high-chirality nodes lie beyond the scope of the present analysis, they suggest promising avenues for future investigation.

IV. FERMI ARC

In K_4 crystal, the presence of Weyl points gives rise to topological surface states—so-called Fermi arcs—that appear when we consider a system with surfaces. We first briefly review the origin of Fermi arcs in conventional Weyl semimetals, and then discuss the characteristic features of those in the K_4 crystal.

A. Conventional Weyl semimetals and Fermi arcs

In conventional Weyl semimetals, pairs of Weyl points with opposite chirality are connected by surface states known as Fermi arcs [17, 20]. Their topological origin can be understood by considering a two-dimensional cylindrical subsystem in momentum space. The cylinder is oriented perpendicular to

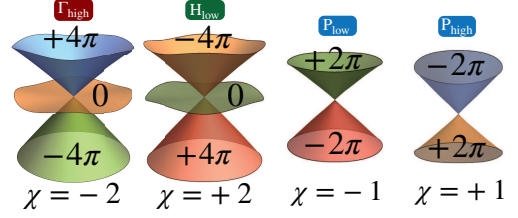


FIG. 2. Energy dispersion around Weyl points in K_4 crystal. At the Γ_{high} and H_{low} points, two conical dispersions and one flat band intersect at a single point, forming what is referred to as a **triple Dirac cone**. The topological charge is calculated for each band, and the sign of the charge associated with the lowest band determines the chirality of the degeneracy point. At the Γ_{high} point, the chirality is $\chi = -2$, while at the H_{low} point, it is $\chi = +2$. At the P_{low} and P_{high} point, two conical bands intersect, forming what are referred to as **simple Dirac cones**, each carrying opposite chirality: $\chi = -1$ at P_{low} and $\chi = +1$ at P_{high} .

the slab Brillouin zone (BZ), for example along k_z in a (001) slab geometry, and encloses a single Weyl point in the bulk BZ. On this cylindrical manifold, the energy spectrum is fully gapped except at the enclosed Weyl point. The Chern number [68, 74] defined on the cylinder equals the chirality of the Weyl point, provided that no other nodes lie within it. If multiple Weyl points are enclosed, the Chern number reflects the sum of their chiralities. When this nonzero Chern number is projected onto the slab BZ, the resulting topologically protected edge states [1, 75] manifest as Fermi arcs that terminate at the projections of Weyl points with opposite chirality.

B. Fermi arcs in the K_4 crystal

We next examine the Fermi arcs that emerge in the K_4 crystal, which connect Weyl points carrying large topological charges. To analyze these surface states, we construct a slab geometry by cleaving the bulk crystal along the xy plane, as illustrated in Fig. 3(a). The three-dimensional bulk BZ is projected onto a two-dimensional slab BZ, as shown in Fig. 3(b). The projections of bulk Weyl points onto the slab BZ are summarized in Table II. The Γ_{high} and H_{low} points project onto the surface $\bar{\Gamma}$ point, while P_{low} and P_{high} project onto \bar{R} . As shown in Fig. 3(c), the bulk gap between the upper two bands closes at the Γ_{high} , P_{high} , and P'_{high} points. Consequently, Fermi arcs emerge across this energy range in the slab system.

The subsystem surrounding the $\bar{\Gamma}$ point reflects the chirality projected from the bulk Γ_{high} point. Owing to the presence of a triple Dirac cone at Γ_{high} with chirality $\chi = -2$, the resulting 2D subsystem acquires a higher Chern number of $C = -2$. On the other hand, the subsystem centered at the \bar{R} point encloses the projected Weyl points at P_{high} and P'_{high} , each with chirality $\chi = +1$, yielding a total Chern number $C = +2$ for this subsystem. These nonzero Chern numbers ensure the existence of Fermi arc surface states crossing the gap, connecting $\bar{\Gamma}$ and \bar{R} points via projected Weyl nodes.

Similarly, the gap between the lower two bands closes at

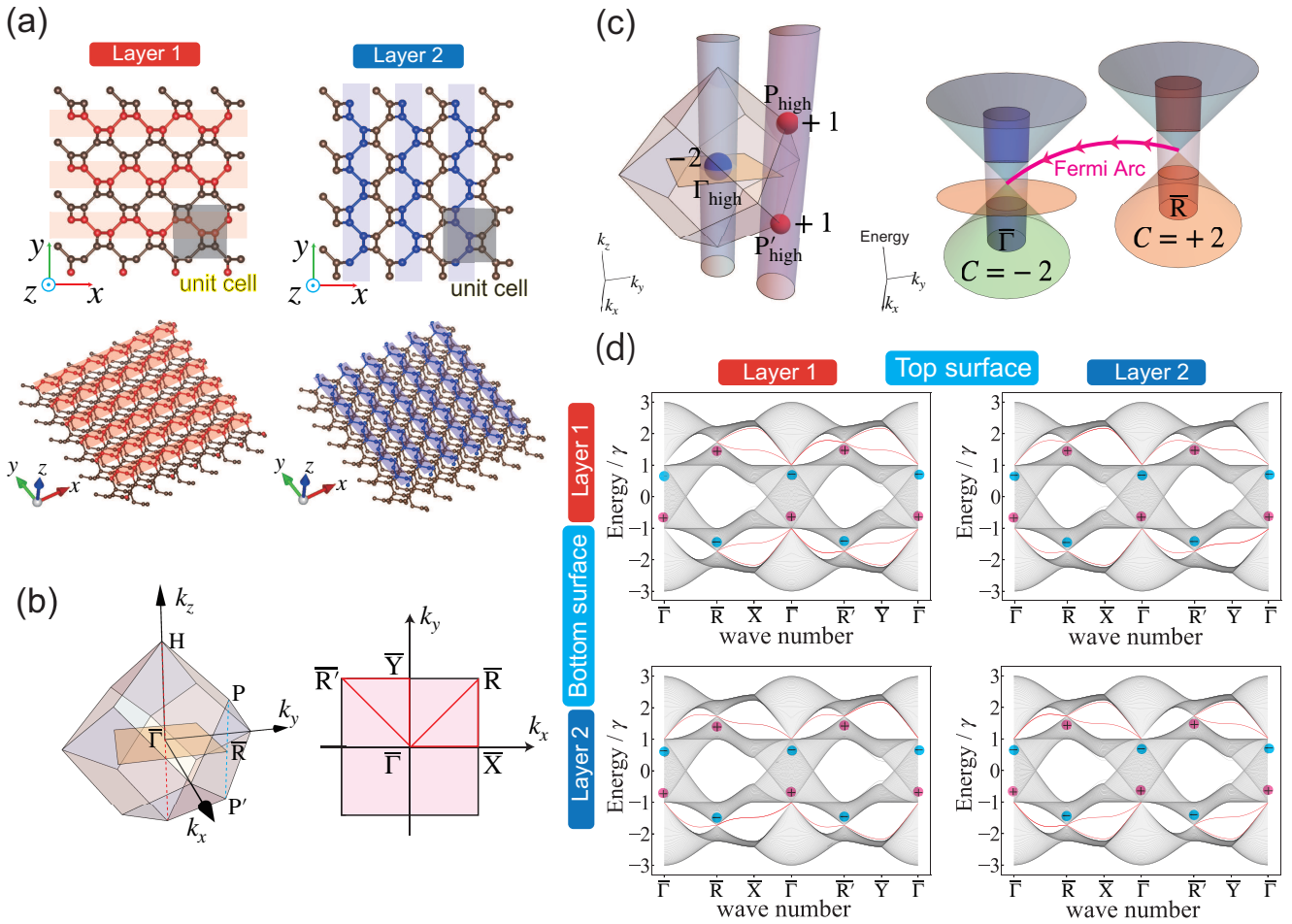


FIG. 3. (a) Slab structure of the K_4 crystal cleaved along (001). Two different types of surface structures: (left) Layer 1 (red) forms chains along the x -axis, and (right) Layer 2 (blue) along the y -axis. Top and perspective views are shown in the upper and lower panels, respectively. Thus, for the slab structures, there are totally four combinations of possible surface terminations. (b) 1st BZ for Bulk and slab structures. (left) 1st BZ of bulk structure, with the yellow square indicating the slab BZ obtained by projecting along the k_z -direction. (right) 1st BZ of slab structures. $\bar{\Gamma}$ corresponds to the projection of the bulk Γ and H points, while \bar{R} correspond to projections of the bulk P and P' points. (c) Left panel schematically shows the bulk BZ, where Γ_{high} (blue sphere) carries chirality $\chi = -2$, and P_{high} and P'_{high} (red spheres) each carry $\chi = +1$. These Weyl nodes are enclosed by distinct momentum-space subsystems: Γ_{high} by a cylinder centered at $\bar{\Gamma}$ (blue), and P_{high} and P'_{high} by a cylinder centered at \bar{R} (red). Accordingly, the subsystem centered at $\bar{\Gamma}$ acquires a Chern number $C = -2$, while that centered at \bar{R} acquires $C = +2$. Right panel shows the energy band structures of slab at $\bar{\Gamma}$ and \bar{R} , respectively. In both cases, the subsystems cut through Weyl cones, yielding effectively two-dimensional systems with energy gaps that host nontrivial Chern numbers. Consequently, topologically protected edge states traverse these gaps. Since the bulk gap closes only at the Weyl nodes, the surface states connect their projections, forming a Fermi arc (pink line) that extends from \bar{R} ($C = +2$) to $\bar{\Gamma}$ ($C = -2$). (d) Energy dispersion of slab structures obtained from the tight-binding model. Gray shading indicates the bulk projection, and red curves highlight the Fermi arcs. Weyl points are labeled by their chiralities. High-energy arcs connect the projected Γ_{high} ($\chi = -2$) to P_{high} and P'_{high} ($\chi = +1 \times 2$), while low-energy arcs connect the projected H_{low} ($\chi = +2$) to P_{low} and P'_{low} ($\chi = -1 \times 2$). The apparent chirality imbalance is resolved by accounting for the projection of symmetry-equivalent Weyl points in the bulk.

H_{low} , P_{low} , and P'_{low} points. Here, H_{low} is projected onto $\bar{\Gamma}$, forming a subsystem with $C = +2$, while P_{low} and P'_{low} project onto \bar{R} , contributing $C = -2$ in total. Fermi arcs also appear between these projections in the lower energy sector.

These features were confirmed by calculating the slab band structures using the tight-binding model. As shown in Fig. 3(a), the (001) slab consists of alternating layers, allowing for four different slab terminations depending on which layer appears on each surface. Figure 3(d) displays the band struc-

tures of all four terminations. In each case, Fermi arcs appear in both the high-energy region ($E > 0$), connecting Γ_{high} to P_{high} and P'_{high} , and the low-energy region ($E < 0$), connecting H_{low} to P_{low} and P'_{low} .

A key distinction from conventional Weyl systems is that one end of a Fermi arc attaches to a triple Dirac cone with chirality $\chi = \pm 2$, while the other end splits into two projected Weyl nodes with $\chi = \mp 1$, preserving overall charge neutrality. Thus, a single arc pair involves three Weyl nodes at different

energies. Because these arcs are topologically protected, they persist even when Weyl nodes acquire small gaps, providing a route to higher-mobility surface states and potential device applications based on higher Chern numbers $C = \pm 2$.

TABLE II. Weyl points (bulk) and their projections onto slab BZ

Weyl Point (bulk)	Γ_{high}	H_{low}	P_{low}	P_{high}
Projected Point in Slab BZ	$\bar{\Gamma}$	$\bar{\Gamma}$	\bar{R}	\bar{R}
Energy	$+\gamma$	$-\gamma$	$-\sqrt{3}\gamma$	$+\sqrt{3}\gamma$
Chirality χ	-2	+2	-1	+1
Symmetry Multiplicity	1	1	2	2

V. SUMMARY

We have investigated the topological electronic properties of the K_4 crystal, a three-dimensional analogue of graphene, by constructing a tight-binding model and analyzing its band structure. The bulk Brillouin zone (BZ) hosts triple band degeneracies at Γ_{high} and H_{low} , comprising two linearly dispersing bands and one flat band-forming what is known as a triple Dirac cone. In contrast, double degeneracies occur at P_{low} and P_{high} , resulting in conventional Dirac cones.

These degeneracy points act as Weyl nodes characterized by isotropic Berry curvature and quantized topological charge (chirality): $\chi = -2$ and $+2$ at Γ_{high} and H_{low} , and $\chi = -1$ and $+1$ at P_{low} and P_{high} , respectively.

To examine the associated surface states, we constructed a slab geometry by cleaving the bulk crystal along the (001) direction. In this configuration, the Weyl nodes at Γ_{high} and H_{low} project onto the surface $\bar{\Gamma}$ point, while those at P_{low} and P_{high} project onto \bar{R} . Although the Fermi arcs appear to connect Weyl points with unbalanced chiralities, this apparent asymmetry is resolved by the presence of two symmetry-equivalent P_{low} or P_{high} points, which effectively double the projected chirality at \bar{R} . This restores the topological charge balance between $\bar{\Gamma}$ and \bar{R} .

Consequently, surface states in the form of Fermi arcs emerge, linking the triple Dirac cone to pairs of simple Dirac cones in a topologically consistent manner. Our results establish the K_4 crystal as a novel Weyl semimetal where higher-chirality nodes are compensated by multiple lower-chirality ones, with their projections robustly connected by topologically protected surface states. This work highlights the K_4 crystal as an archetype of three-dimensional sp^2 carbon networks with intrinsic topological properties, providing a foundation for future exploration of higher-chirality fermions and their potential applications in topological electronics.

Further experimental validation of the predicted topological phenomena in the K_4 crystal will be essential. For instance, angle-resolved photoemission spectroscopy (ARPES) and quantum-oscillation measurements have already observed Fermi arcs and Berry phase signatures in Weyl semimetals such as TaAs (Refs. [76–79]) and large-Chern-number systems like PtGa (Ref. [80]). Drawing on these precedents,

similar techniques could be applied once a realisation of the K_4 crystal becomes available. Additionally, photonic-crystal analogues of the triple-degenerate point have recently been demonstrated in acoustic/photonic systems (for example, Refs. [51, 81]), suggesting that the K_4 lattice-with its inherent higher-chirality fermions could serve as a prototype not only for electronic topological materials but also for topological photonics and metamaterials.

Looking ahead, an intriguing direction is to determine whether the chirality and the Berry curvature of the nodal points can be derived purely from crystal symmetry, for example through symmetry indicators or irreducible-representation analysis. Establishing such a connection would not only reinforce the topological robustness of the observed nodes, but also enable a deeper symmetry-based classification of topological semimetals in nonsymmorphic crystals such as the K_4 lattice.

ACKNOWLEDGMENTS

This work was supported by JSPS KAKENHI (Grants No. JP25K01609, No. JP22H05473, and No. JP21H01019), JST CREST (Grant No. JPMJCR19T1). K.W. acknowledges the financial support for Basic Science Research Projects (Grant No. 2401203) from the Sumitomo Foundation.

DATA AVAILABILITY

The data used and analyzed during the current study available from corresponding authors on reasonable request.

Appendix A: Topological properties at H_{low} , P_{low} , P_{high} points

In this section, we provide the derivations of the topological quantities such as Berry connection, Berry curvature and topological charges at H_{low} , P_{high} , and P_{low} points.

1. H_{low} point

Expanding the tight-binding Hamiltonian [Eq. (1)] to first order in momentum \mathbf{k} around the H point, i.e., $\mathbf{k}_H = (0, \frac{2\pi}{a}, 0)$, the effective Hamiltonian can be written as

$$H_H^{(1)}(\mathbf{k}) = -\gamma \begin{pmatrix} 0 & -i & 1 & i \\ i & 0 & -i & 1 \\ 1 & i & 0 & -i \\ -i & 1 & i & 0 \end{pmatrix} - \frac{\gamma a}{4} \begin{pmatrix} 0 & -(k_y - k_z) & -i(k_z - k_x) & (k_x - k_y) \\ -(k_y - k_z) & 0 & -(k_x + k_y) & -i(-k_z - k_x) \\ i(k_z - k_x) & -(k_x + k_y) & 0 & -(k_y + k_z) \\ (k_x - k_y) & i(-k_z - k_x) & -(k_y + k_z) & 0 \end{pmatrix}.$$

This Hamiltonian can be block-diagonalized using a unitary matrix U_H , as

$$U_H^\dagger H_H^{(1)}(\mathbf{k}) U_H = -\gamma \begin{pmatrix} -3 & 0 & 0 & 0 \\ 0 & 1 & 0 & 0 \\ 0 & 0 & 1 & 0 \\ 0 & 0 & 0 & 1 \end{pmatrix} + \frac{\gamma a}{2} \begin{pmatrix} 0 & 0 & 0 & 0 \\ 0 & k_z & \frac{1}{\sqrt{2}}k_- & 0 \\ 0 & \frac{1}{\sqrt{2}}k_+ & 0 & \frac{1}{\sqrt{2}}k_- \\ 0 & 0 & \frac{1}{\sqrt{2}}k_+ & -k_z \end{pmatrix},$$

where $k = \sqrt{k_x^2 + k_y^2 + k_z^2}$ and $k_{\pm} = k_x \pm ik_y$.

The unitary matrix U_H can be given as

$$U_H = \frac{1}{2} \begin{pmatrix} -i & e^{-i\frac{3\pi}{4}} & 1 & e^{-i\frac{\pi}{4}} \\ -1 & e^{i\frac{\pi}{4}} & i & e^{-i\frac{\pi}{4}} \\ i & e^{i\frac{3\pi}{4}} & 1 & e^{i\frac{\pi}{4}} \\ 1 & e^{i\frac{3\pi}{4}} & i & e^{-i\frac{3\pi}{4}} \end{pmatrix}.$$

By discarding the term concerning the flat band ($+3\gamma$), we obtain an effective three-band Hamiltonian near the H_{low} point:

$$H_{H_{\text{low}},\text{eff}}(\mathbf{k}) = +\frac{\gamma a}{2} \begin{pmatrix} k_z & \frac{1}{\sqrt{2}}k_- & 0 \\ \frac{1}{\sqrt{2}}k_+ & 0 & \frac{1}{\sqrt{2}}k_- \\ 0 & \frac{1}{\sqrt{2}}k_+ & -k_z \end{pmatrix}.$$

This effective Hamiltonian can be expressed in a compact form as

$$H_{H_{\text{low}},\text{eff}}(\mathbf{k}) = +\frac{\gamma a}{2} \mathbf{k} \cdot \mathbf{S}. \quad (\text{A1})$$

This Hamiltonian is the sign-reversed counterpart of the effective Hamiltonian at the Γ_{high} point [Eq. (3)]. Its eigenvalues are

$$E_{H_{\text{low}}}^- = \frac{-\gamma a}{2} k, \quad E_{H_{\text{low}}}^0 = 0, \quad E_{H_{\text{low}}}^+ = \frac{+\gamma a}{2} k,$$

which are identical to those at the Γ_{high} point.

These correspond to a lower conical band, a flat central band, and an upper conical band, which meet at the H_{low} point to form a *triple Dirac cone*, as illustrated in Fig. 2 (the H_{low} point).

However, the eigenspaces corresponding to the upper and lower conical bands at H_{low} are reversed compared to those at Γ_{high} . The normalized eigenfunctions are given by

$$\begin{aligned} \mathbf{u}_{H_{\text{low}}}^- &= \frac{1}{2k(k_z - k)} \begin{pmatrix} (k_z - k)^2 \\ \sqrt{2}k_+(k_z - k) \\ k_+^2 \end{pmatrix}, \\ \mathbf{u}_{H_{\text{low}}}^0 &= \frac{1}{\sqrt{2}k} \begin{pmatrix} -k_- \\ \sqrt{2}k_z \\ k_+ \end{pmatrix}, \\ \mathbf{u}_{H_{\text{low}}}^+ &= \frac{1}{2k(k_z + k)} \begin{pmatrix} (k_z + k)^2 \\ \sqrt{2}k_+(k_z + k) \\ k_+^2 \end{pmatrix}. \end{aligned}$$

As a result, the Berry connections and Berry curvatures for these bands are also interchanged.

The Berry connections are

$$A_{H_{\text{low}}}^- = \frac{1}{k(k_z - k)} \begin{pmatrix} -k_y \\ k_x \\ 0 \end{pmatrix},$$

$$A_{H_{\text{low}}}^0 = \mathbf{0},$$

$$A_{H_{\text{low}}}^+ = \frac{1}{k(k_z + k)} \begin{pmatrix} k_y \\ -k_x \\ 0 \end{pmatrix},$$

and the corresponding Berry curvatures are

$$\Omega_{H_{\text{low}}}^- = \frac{+k}{k^3}, \quad \Omega_{H_{\text{low}}}^0 = \mathbf{0}, \quad \Omega_{H_{\text{low}}}^+ = \frac{-k}{k^3}.$$

The monopole charges associated with each band are then given by

$$\phi_{H_{\text{low}}}^- = +4\pi, \quad \phi_{H_{\text{low}}}^0 = 0, \quad \phi_{H_{\text{low}}}^+ = -4\pi.$$

Thus, the Γ_{high} and H_{low} points not only share the same band structure form but also exhibit opposite topological characteristics, forming a pair in both energy and topology.

2. P_{low} point and P_{high} point

The Hamiltonian matrix [Eq. (1)] is expanded up to first order in momentum \mathbf{k} around the P point, $\mathbf{k}_P = (\frac{\pi}{a}, \frac{\pi}{a}, \frac{\pi}{a})$, as

$$H_P^{(1)}(\mathbf{k}) = -\gamma \begin{pmatrix} 0 & 1 & 1 & 1 \\ 1 & 0 & -i & i \\ 1 & i & 0 & -i \\ 1 & -i & i & 0 \end{pmatrix} - \frac{\gamma a}{4} \begin{pmatrix} 0 & -i(k_y - k_z) & -i(k_z - k_x) & -i(k_x - k_y) \\ i(k_y - k_z) & 0 & -(k_x + k_y) & -(-k_z - k_x) \\ i(k_z - k_x) & -(k_x + k_y) & 0 & -(k_y + k_z) \\ i(k_x - k_y) & -(-k_z - k_x) & -(k_y + k_z) & 0 \end{pmatrix}.$$

Although this Hamiltonian cannot be fully block-diagonalized by a unitary transformation, we consider the unitary matrix

$$U_P = \frac{1}{\sqrt{6}} \begin{pmatrix} \sqrt{3} & 0 & -\sqrt{3} & 0 \\ 1 & \sqrt{2}\omega & 1 & \sqrt{2}\omega^2 \\ 1 & \sqrt{2}\omega^2 & 1 & \sqrt{2}\omega \\ 1 & \sqrt{2} & 1 & \sqrt{2} \end{pmatrix},$$

where $\omega = \frac{-1+i\sqrt{3}}{2}$, $\omega^3 = 1$. This unitary matrix diagonal-

lizes the zeroth-order part of $H_P^{(1)}(\mathbf{k})$, i.e., the Hamiltonian at the P point itself.

By applying this transformation, we obtain

$$U_P^\dagger H_P^{(1)}(\mathbf{k}) U_P = \begin{pmatrix} -\sqrt{3}\gamma & 0 & 0 & 0 \\ 0 & -\sqrt{3}\gamma & 0 & 0 \\ 0 & 0 & +\sqrt{3}\gamma & 0 \\ 0 & 0 & 0 & +\sqrt{3}\gamma \end{pmatrix} + \delta H_P(\mathbf{k}),$$

where $\delta H_P(\mathbf{k})$ contains all the first-order terms:

$$\delta H_P(\mathbf{k}) = \begin{pmatrix} k_x + k_y + k_z & \sqrt{2}(\omega k_x + \omega^2 k_y + k_z) & k_x + k_y + k_z & \frac{1}{\sqrt{2}}(-\omega^2 k_x - \omega k_y - k_z) \\ \sqrt{2}(\omega^2 k_x + \omega k_y + k_z) & -k_x - k_y - k_z & \frac{1}{\sqrt{2}}(-\omega^2 k_x - \omega k_y - k_z) & -\omega k_x - \omega^2 k_y - k_z \\ k_x + k_y + k_z & \frac{1}{\sqrt{2}}(-\omega k_x - \omega^2 k_y - k_z) & k_x + k_y + k_z & \sqrt{2}(\omega^2 k_x + \omega k_y + k_z) \\ \frac{1}{\sqrt{2}}(-\omega k_x - \omega^2 k_y - k_z) & -\omega^2 k_x - \omega k_y - k_z & \sqrt{2}(\omega k_x + \omega^2 k_y + k_z) & -k_x - k_y - k_z \end{pmatrix},$$

which are not block-diagonalized by U_P .

In contrast to the cases at the Γ and H points, the first-order correction $\delta H_P(\mathbf{k})$ is not diagonal in this transformed basis. However, since the zeroth-order Hamiltonian has a two-fold degenerate low-energy sector $(-\sqrt{3}\gamma)$ and high-energy sector $(+\sqrt{3}\gamma)$, and the energy splitting is finite at $\mathbf{k} = 0$, we may

treat these sectors separately in the vicinity of the P point.

Thus, by neglecting the off-diagonal coupling between the low-energy and high-energy subspaces in $\delta H_P(\mathbf{k})$, we obtain two effective 2×2 Hamiltonians. The upper-left 2×2 block corresponds to the low-energy effective Hamiltonian at the P_{low} point, and the lower-right 2×2 block corresponds to the

high-energy effective Hamiltonian at the P_{high} point.

The effective Hamiltonians are given by:

$$H_{P_{\text{low}},\text{eff}}(\mathbf{k}) = +\frac{\gamma a}{6} \begin{pmatrix} k_x + k_y + k_z & \sqrt{2}(\omega k_x + \omega^2 k_y + k_z) \\ \sqrt{2}(\omega^2 k_x + \omega k_y + k_z) & -k_x - k_y - k_z \end{pmatrix},$$

$$H_{P_{\text{high}},\text{eff}}(\mathbf{k}) = +\frac{\gamma a}{6} \begin{pmatrix} k_x + k_y + k_z & \sqrt{2}(\omega^2 k_x + \omega k_y + k_z) \\ \sqrt{2}(\omega k_x + \omega^2 k_y + k_z) & -k_x - k_y - k_z \end{pmatrix}.$$

The eigenvalues of the effective Hamiltonian $H_{P_{\text{low}},\text{eff}}(\mathbf{k})$ are given by

$$E_{P_{\text{low}}}^{\pm} = \pm \frac{\gamma a}{2\sqrt{3}} k,$$

which describe a pair of conically dispersing bands meeting at the P_{low} point, thereby forming a simple Dirac cone, as shown in Fig. 2 (P_{low}).

The corresponding normalized eigenvectors are

$$\mathbf{u}_{P_{\text{low}}}^{-} = \frac{1}{\eta_{-}} \begin{pmatrix} \frac{1}{\sqrt{2}}(k_x + k_y + k_z - \sqrt{3}k) \\ \omega^2 k_x + \omega k_y + k_z \end{pmatrix},$$

$$\mathbf{u}_{P_{\text{low}}}^{+} = \frac{1}{\eta_{+}} \begin{pmatrix} \frac{1}{\sqrt{2}}(k_x + k_y + k_z + \sqrt{3}k) \\ \omega^2 k_x + \omega k_y + k_z \end{pmatrix},$$

$$\text{where } \eta_{\pm} = \sqrt{\sqrt{3}k(\sqrt{3}k \pm k_x \pm k_y \pm k_z)}.$$

From these eigenstates, the Berry connections are computed as

$$\mathbf{A}_{P_{\text{low}}}^{-} = \frac{1}{2k(k_x + k_y + k_z - \sqrt{3}k)} \begin{pmatrix} k_y - k_z \\ k_z - k_x \\ k_x - k_y \end{pmatrix},$$

$$\mathbf{A}_{P_{\text{low}}}^{+} = \frac{1}{2k(k_x + k_y + k_z + \sqrt{3}k)} \begin{pmatrix} -k_y + k_z \\ -k_z + k_x \\ -k_x + k_y \end{pmatrix}.$$

The corresponding Berry curvatures take the form

$$\Omega_{P_{\text{low}}}^{-} = \frac{-\mathbf{k}}{2k^3}, \quad \Omega_{P_{\text{low}}}^{+} = \frac{+\mathbf{k}}{2k^3}.$$

These expressions indicate that the P_{low} point carries monopole-type Berry curvature, with magnitude equal to half of those found at the Γ_{high} and H_{low} points for the upper and lower cones.

Accordingly, the topological charges are given by

$$\phi_{P_{\text{low}}}^{-} = -2\pi, \quad \phi_{P_{\text{low}}}^{+} = +2\pi.$$

The P_{high} point serves as the counterpart to the P_{low} point. In contrast to the Γ_{high} and H_{low} points, where the upper and lower conical bands exchange their eigenspaces, the eigenspaces of the conical bands at the P_{high} and P_{low} points are related by complex conjugation. Consequently, the Berry connections and Berry curvatures at the P_{high} point are also complex conjugates of those at the P_{low} point, leading to opposite topological charges.

The eigenvalues of the effective Hamiltonian $H_{P_{\text{high}},\text{eff}}(\mathbf{k})$ are given by

$$E_{P_{\text{high}}}^{\pm} = \pm \frac{\gamma a}{2\sqrt{3}} k,$$

which correspond to a pair of conical bands forming a simple Dirac cone at the P_{high} point, as shown in Fig. 2 (P_{high}).

The normalized eigenfunctions are

$$\mathbf{u}_{P_{\text{high}}}^{-} = \frac{1}{\eta_{-}} \begin{pmatrix} \frac{1}{\sqrt{2}}(k_x + k_y + k_z - \sqrt{3}k) \\ \omega k_x + \omega^2 k_y + k_z \end{pmatrix},$$

$$\mathbf{u}_{P_{\text{high}}}^{+} = \frac{1}{\eta_{+}} \begin{pmatrix} \frac{1}{\sqrt{2}}(k_x + k_y + k_z + \sqrt{3}k) \\ \omega k_x + \omega^2 k_y + k_z \end{pmatrix}.$$

The corresponding Berry connections are

$$\mathbf{A}_{P_{\text{high}}}^{-} = \frac{1}{2k(k_x + k_y + k_z - \sqrt{3}k)} \begin{pmatrix} -k_y + k_z \\ -k_z + k_x \\ -k_x + k_y \end{pmatrix},$$

$$\mathbf{A}_{P_{\text{high}}}^{+} = \frac{1}{2k(k_x + k_y + k_z + \sqrt{3}k)} \begin{pmatrix} k_y - k_z \\ k_z - k_x \\ k_x - k_y \end{pmatrix},$$

and the associated Berry curvatures are

$$\Omega_{P_{\text{high}}}^{-} = \frac{+\mathbf{k}}{2k^3}, \quad \Omega_{P_{\text{high}}}^{+} = \frac{-\mathbf{k}}{2k^3}.$$

Accordingly, the topological charges at the P_{high} point are

given by

$$\phi_{P_{\text{high}}}^- = +2\pi, \quad \phi_{P_{\text{high}}}^+ = -2\pi,$$

which are the reverse of those found at the P_{low} point.

[1] C. L. Kane and E. J. Mele, Quantum spin hall effect in graphene, *Phys. Rev. Lett.* **95**, 226801 (2005).

[2] B. A. Bernevig, T. L. Hughes, and S.-C. Zhang, Quantum spin hall effect and topological phase transition in hgte quantum wells, *Science* **314**, 1757 (2006).

[3] L. Fu, C. L. Kane, and E. J. Mele, Topological insulators in three dimensions, *Phys. Rev. Lett.* **98**, 106803 (2007).

[4] M. König, S. Wiedmann, C. Brüne, A. Roth, H. Buhmann, L. W. Molenkamp, X.-L. Qi, and S.-C. Zhang, Quantum spin hall insulator state in hgte quantum wells, *Science* **318**, 766 (2007).

[5] X.-L. Qi and S.-C. Zhang, Topological insulators and superconductors, *Rev. Mod. Phys.* **83**, 1057 (2011).

[6] D. Hsieh, D. Qian, L. Wray, Y. Xia, Y. S. Hor, R. J. Cava, and M. Z. Hasan, A topological dirac insulator in a quantum spin hall phase, *Nature* **452**, 970 (2008).

[7] Y. L. Chen, J. G. Analytis, J.-H. Chu, Z. K. Liu, S.-K. Mo, X. L. Qi, H. J. Zhang, D. H. Lu, X. Dai, Z. Fang, S. C. Zhang, I. R. Fisher, Z. Hussain, and Z.-X. Shen, Experimental realization of a three-dimensional topological insulator, $\text{bi}_{1-x}\text{sub}_2\text{te}_1\text{sub}_3\text{sub}_2$, *Science* **325**, 178 (2009).

[8] C.-Z. Chang, J. Zhang, X. Feng, J. Shen, Z. Zhang, M. Guo, K. Li, Y. Ou, P. Wei, L.-L. Wang, Z.-Q. Ji, Y. Feng, S. Ji, X. Chen, J. Jia, X. Dai, Z. Fang, S.-C. Zhang, K. He, Y. Wang, L. Lu, X.-C. Ma, and Q.-K. Xue, Experimental observation of the quantum anomalous hall effect in a magnetic topological insulator, *Science* **340**, 167 (2013).

[9] Y. Ando, Topological insulator materials, *J. Phys. Soc. Jpn.* **82**, 102001 (2013).

[10] M. Z. Hasan and C. L. Kane, Colloquium: Topological insulators, *Rev. Mod. Phys.* **82**, 3045 (2010).

[11] X.-L. Qi and S.-C. Zhang, The quantum spin hall effect and topological insulators, *Physics Today* **63**, 33 (2010).

[12] Y. Zhang, K. He, C.-Z. Chang, C.-L. Song, L.-L. Wang, X. Chen, J.-F. Jia, Z. Fang, X. Dai, W.-Y. Shan, S.-Q. Shen, Q. Niu, X.-L. Qi, S.-C. Zhang, X.-C. Ma, and Q.-K. Xue, Crossover of the three-dimensional topological insulator bi_2se_3 to the two-dimensional limit, *Nat. Phys.* **6**, 584 (2010).

[13] L. Fu, Topological crystalline insulators, *Phys. Rev. Lett.* **106**, 106802 (2011).

[14] T. H. Hsieh, H. Lin, J. Liu, W. Duan, A. Bansil, and L. Fu, Topological crystalline insulators in the SnTe material class, *Nat. Commun.* **3**, 982 (2012).

[15] Y. Tokura, K. Yasuda, and A. Tsukazaki, Magnetic topological insulators, *Nat. Rev. Phys.* **1**, 126 (2019).

[16] R. S. K. Mong, A. M. Essin, and J. E. Moore, Antiferromagnetic topological insulators, *Phys. Rev. B* **81**, 245209 (2010).

[17] X. Wan, A. M. Turner, A. Vishwanath, and S. Y. Savrasov, Topological semimetal and fermi-arc surface states in the electronic structure of pyrochlore iridates, *Phys. Rev. B* **83**, 205101 (2011).

[18] S.-Y. Xu, I. Belopolski, N. Alidoust, M. Neupane, G. Bian, C. Zhang, R. Sankar, G. Chang, Z. Yuan, C.-C. Lee, S.-M. Huang, H. Zheng, J. Ma, D. S. Sanchez, B. Wang, A. Bansil, F. Chou, P. P. Shibayev, H. Lin, S. Jia, and M. Z. Hasan, Discovery of a weyl fermion semimetal and topological fermi arcs, *Science* **349**, 613 (2015).

[19] Z. Wang, Y. Sun, X.-Q. Chen, C. Franchini, G. Xu, H. Weng, X. Dai, and Z. Fang, Dirac semimetal and topological phase transitions in a3bi ($\text{a}=\text{na, k, rb}$), *Phys. Rev. B* **85**, 195320 (2012).

[20] N. P. Armitage, E. J. Mele, and A. Vishwanath, Weyl and dirac semimetals in three-dimensional solids, *Rev. Mod. Phys.* **90**, 015001 (2018).

[21] K. Deng, G. Wan, P. Deng, K. Zhang, S. Ding, E. Wang, M. Yan, H. Huang, H. Zhang, Z. Xu, J. Denlinger, A. Fedorov, H. Yang, W. Duan, H. Yao, Y. Wu, S. Fan, H. Zhang, X. Chen, and S. Zhou, Experimental observation of topological fermi arcs in type-II weyl semimetal MoTe_2 , *Nat. Phys.* **12**, 1105 (2016).

[22] T. Sunada, Crystals that nature might miss creating, *Notices of the American Mathematical Society* **55**, 208 (2008).

[23] T. Sunada, *Topological Crystallography* (Springer, 2013).

[24] T. Sunada, Diamond twin, arXiv 10.48550/arxiv.1904.07230 (2019).

[25] T. Sunada, Lecture on topological crystallography, *Jpn. J. Math.* **7**, 1 (2012).

[26] M. O'Keeffe, M. A. Peskov, S. J. Ramsden, and O. M. Yaghi, The reticular chemistry structure resource (RCSR) database of, and symbols for, crystal nets, *Acc. Chem. Res.* **41**, 1782 (2008).

[27] S. T. Hyde, M. O'Keeffe, and D. M. Proserpio, A short history of an elusive yet ubiquitous structure in chemistry, materials, and mathematics, *Angew. Chem. Int. Ed.* **47**, 7996 (2008).

[28] K. Michielsen and D. Stavenga, Gyroid cuticular structures in butterfly wing scales: biological photonic crystals, *J. R. Soc. Interface* **5**, 85 (2008).

[29] M. Itoh, M. Kotani, H. Naito, T. Sunada, Y. Kawazoe, and T. Adschiri, New metallic carbon crystal, *Phys. Rev. Lett.* **102**, 055703 (2009).

[30] M. Tsuchizawa, Three-dimensional higher-spin dirac and weyl dispersions in the strongly isotropic k4 crystal, *Phys. Rev. B* **94**, 195426 (2016).

[31] K. Hagita, R. Sahara, and Y. Kawazoe, DFT study of carbon crystals from nested k4 lattice to BC-8 structure, *J. Chin. Chem. Soc.* **63**, 526 (2016).

[32] A. H. Castro Neto, F. Guinea, N. M. R. Peres, K. S. Novoselov, and A. K. Geim, The electronic properties of graphene, *Rev. Mod. Phys.* **81**, 109 (2009).

[33] K. S. Novoselov, A. K. Geim, S. V. Morozov, D. Jiang, M. I. Katsnelson, I. V. Grigorieva, S. V. Dubonos, and A. A. Firsov, Two-dimensional gas of massless Dirac fermions in graphene, *Nature* **438**, 197 (2005).

[34] Y. Zhang, Y.-W. Tan, H. L. Stormer, and P. Kim, Experimental observation of the quantum Hall effect and Berry's phase in graphene, *Nature* **438**, 201 (2005).

[35] C. J. Wort and R. S. Balmer, Diamond as an electronic material, *Materials Today* **11**, 22 (2008).

[36] N. Mounet and N. Marzari, First-principles determination of

the structural, vibrational and thermodynamic properties of diamond, graphite, and derivatives, *Phys. Rev. B* **71**, 205214 (2005).

[37] J. Dai, Z. Li, and J. Yang, Boron k 4 crystal: a stable chiral three-dimensional sp 2 network, *Phys. Chem. Chem. Phys.* **12**, 12420 (2010).

[38] J. Liu, S. Zhang, Y. Guo, and Q. Wang, Phosphorus k4 crystal: A new stable allotrope, *Sci. Rep.* **6**, 37528 (2016).

[39] C.-S. Lian, X.-Q. Wang, and J.-T. Wang, Hydrogenated k4 carbon: A new stable cubic gauche structure of carbon hydride, *J. Chem. Phys.* **138**, 024702 (2013).

[40] B. Wen, S. Takami, Y. Kawazoe, and T. Adschiri, Carbon-doped k4 nitrogen: A novel high energy density material, *Chem. Phys. Lett.* **506**, 175 (2011).

[41] B. Wen, S. Takami, Y. Kawazoe, and T. Adschiri, Mechanical stabilities of k4 carbon and k4-like NaC2, *Journal of Physics and Chemistry of Solids* **73**, 1264 (2012).

[42] A. Mizuno, Y. Shuku, R. Suizu, M. M. Matsushita, M. Tsuchizawa, D. Reta Mañeru, F. Illas, V. Robert, and K. Awaga, Discovery of the K4 Structure Formed by a Triangular π Radical Anion, *J. Am. Chem. Soc.* **137**, 7612 (2015).

[43] B. Bradlyn, J. Cano, Z. Wang, M. G. Vergniory, C. Felser, R. J. Cava, and B. A. Bernevig, Beyond dirac and weyl fermions: Unconventional quasiparticles in conventional crystals, *Science* **353**, aaf5037 (2016).

[44] Z. Zhu, G. W. Winkler, Q. Wu, J. Li, and A. A. Soluyanov, Triple point topological metals, *Phys. Rev. X* **6**, 031003 (2016).

[45] F. Flicker, F. d. Juan, B. Bradlyn, T. Morimoto, M. G. Vergniory, and A. G. Grushin, Chiral optical response of multifold fermions, *Phys. Rev. B* **98**, 155145 (2018).

[46] Y. Wang, W. Yang, W. Shi, W. Liu, and Q. Xu, Exhaustive screening of high-fold degenerate topological semimetal with chiral structure, *npj Comput. Mater.* **11**, 120 (2025).

[47] N. B. M. Schröter, I. Robredo, S. Klemenz, R. J. Kirby, J. A. Krieger, D. Pei, T. Yu, S. Stolz, T. Schmitt, P. Dudin, T. K. Kim, C. Cacho, A. Schnyder, A. Bergara, V. N. Strocov, F. d. Juan, M. G. Vergniory, and L. M. Schoop, Weyl fermions, fermi arcs, and minority-spin carriers in ferromagnetic CoS2, *Sci. Adv.* **6**, eabd5000 (2020).

[48] B. Xu, Z. Fang, M.-A. Sánchez-Martínez, J. W. F. Venderbos, Z. Ni, T. Qiu, K. Manna, K. Wang, J. Paglione, C. Bernhard, C. Felser, E. J. Mele, A. G. Grushin, A. M. Rappe, and L. Wu, Optical signatures of multifold fermions in the chiral topological semimetal CoSi, *Proc. Natl. Acad. Sci. U.S.A.* **117**, 27104 (2020).

[49] H. Hu, J. Hou, F. Zhang, and C. Zhang, Topological triply degenerate points induced by spin-tensor-momentum couplings, *Phys. Rev. Lett.* **120**, 240401 (2018).

[50] I. C. Fulga and A. Stern, Triple point fermions in a minimal symmorphic model, *Phys. Rev. B* **95**, 241116 (2017).

[51] Y. Yang, H.-x. Sun, J.-p. Xia, H. Xue, Z. Gao, Y. Ge, D. Jia, S.-q. Yuan, Y. Chong, and B. Zhang, Topological triply degenerate point with double fermi arcs, *Nat. Phys.* **15**, 645 (2019).

[52] D. Vanderbilt, *Berry Phases in Electronic Structure Theory* (Cambridge University Press, 2018).

[53] D. Xiao, M.-C. Chang, and Q. Niu, Berry phase effects on electronic properties, *Rev. Mod. Phys.* **82**, 1959 (2010).

[54] J. Zak, Berry's phase for energy bands in solids, *Phys. Rev. Lett.* **62**, 2747 (1989).

[55] R. D. King-Smith and D. Vanderbilt, Theory of polarization of crystalline solids, *Phys. Rev. B* **47**, 1651 (1992).

[56] R. Resta, Macroscopic polarization in crystalline dielectrics: the geometric phase approach, *Rev. Mod. Phys.* **66**, 899 (1994).

[57] N. Marzari, A. A. Mostofi, J. R. Yates, I. Souza, and D. Vanderbilt, Maximally localized wannier functions: Theory and applications, *Rev. Mod. Phys.* **84**, 1419 (2012).

[58] Y. Zhou, K. M. Rabe, and D. Vanderbilt, Surface polarization and edge charges, *Phys. Rev. B* **92**, 041102 (2015).

[59] F. Liu and K. Wakabayashi, Novel topological phase with a zero berry curvature, *Phys. Rev. Lett.* **118**, 076803 (2017).

[60] P. Delplace, D. Ullmo, and G. Montambaux, Zak phase and the existence of edge states in graphene, *Phys. Rev. B* **84**, 195452 (2011).

[61] K. Koizumi, H. T. Phan, K. Nishigomi, and K. Wakabayashi, Topological edge and corner states in the biphenylene network, *Phys. Rev. B* **109**, 035431 (2024).

[62] M. I. Aroyo, ed., *International Tables for Crystallography, Volume A: Space-group Symmetry*, 6th ed. (John Wiley & Sons / International Union of Crystallography, Chichester, UK, 2016).

[63] R. W. G. Wyckoff, *Crystal Structures*, 2nd ed., Vol. 1 (Interscience Publishers, New York, 1963) 6 vols. in 7, published 1963–1971.

[64] B. Bradlyn, L. Elcoro, J. Cano, M. G. Vergniory, Z. Wang, C. Felser, M. I. Aroyo, and B. A. Bernevig, Topological quantum chemistry, *Nature* **547**, 298 (2017), 1703.02050.

[65] M. I. Aroyo, J. M. Perez-Mato, D. Orobengoa, E. Tasci, G. de la Flor, and A. Kirov, Bilbao crystallographic server: I. databases and crystallographic computing programs, *Acta Crystallogr. A* **62**, 115 (2006).

[66] H. Weyl, Elektron und gravitation. i, *Zeitschrift für Physik* **56**, 330 (1929).

[67] S. S. Chern and J. Simons, Characteristic forms and geometrical invariants, *Ann. Math.* **100**, 48 (1974).

[68] D. J. Thouless, M. Kohmoto, M. P. Nightingale, and M. d. Nijs, Quantized hall conductance in a two-dimensional periodic potential, *Phys. Rev. Lett.* **49**, 405 (1982).

[69] M. Elbistan, Weyl semimetal and topological numbers, *Int. J. Mod. Phys. B* **31**, 1750221 (2017).

[70] H. Nielsen and M. Ninomiya, Absence of neutrinos on a lattice (i). proof by homotopy theory, *Nucl. Phys. B* **185**, 20 (1981).

[71] H. Nielsen and M. Ninomiya, Absence of neutrinos on a lattice (II). intuitive topological proof, *Nucl. Phys. B* **193**, 173 (1981).

[72] S. S. Tsirkin, I. Souza, and D. Vanderbilt, Composite weyl nodes stabilized by screw symmetry with and without time-reversal invariance, *Physical Review B* **96**, 045102 (2017), 1704.00129.

[73] R. González Hernández, E. Tuiran, and B. Uribe, Chiralities of nodal points along high-symmetry lines with screw rotation symmetry, *Physical Review B* **103**, 235143 (2021), 2102.09970.

[74] M. Kohmoto, Berry's phase of bloch electrons in electromagnetic fields, *J.Phys.Soc.Jpn.* **62**, 659 (1993).

[75] Y. Hatsugai, Chern number and edge states in the integer quantum hall effect, *Phys. Rev. Lett.* **71**, 3697 (1993).

[76] B. Q. Lv, H. M. Weng, B. B. Fu, X. P. Wang, H. Miao, J. Ma, P. Richard, X. C. Huang, L. X. Zhao, G. F. Chen, Z. Fang, X. Dai, T. Qian, and H. Ding, Experimental discovery of weyl semimetal TaAs, *Physical Review X* **5**, 031013 (2015), 1502.04684.

[77] I. Belopolski, S.-Y. Xu, D. S. Sanchez, G. Chang, C. Guo, M. Neupane, H. Zheng, C.-C. Lee, S.-M. Huang, G. Bian, N. Alidoust, T.-R. Chang, B. Wang, X. Zhang, A. Bansil, H.-T. Jeng, H. Lin, S. Jia, and M. Z. Hasan, Criteria for directly detecting topological fermi arcs in weyl semimetals, *Physical Review Letters* **116**, 066802 (2016), 1601.04327.

[78] X. Huang, L. Zhao, Y. Long, P. Wang, D. Chen, Z. Yang, H. Liang, M. Xue, H. Weng, Z. Fang, X. Dai, and G. Chen, Observation of the chiral-anomaly-induced negative magnetoresis-

tance in 3d weyl semimetal TaAs, *Physical Review X* **5**, 031023 (2015), 1503.01304.

[79] J. Hu, J. Y. Liu, D. Graf, S. M. A. Radmanesh, D. J. Adams, A. Chuang, Y. Wang, I. Chiorescu, J. Wei, L. Spinu, and Z. Q. Mao, π berry phase and zeeman splitting of weyl semimetal TaP, *Scientific Reports* **6**, 18674 (2016).

[80] M. Yao, K. Manna, Q. Yang, A. Fedorov, V. Voroshnin, B. V. Schwarze, J. Hornung, S. Chattopadhyay, Z. Sun, S. N. Guin, J. Wosnitza, H. Borrmann, C. Shekhar, N. Kumar, J. Fink, Y. Sun, and C. Felser, Observation of giant spin-split fermi-arc with maximal chern number in the chiral topological semimetal PtGa, *Nature Communications* **11**, 2033 (2020), 2003.07712.

[81] L. Lu, L. Fu, J. D. Joannopoulos, and M. Soljačić, Weyl points and line nodes in gyroid photonic crystals, *Nature Photonics* **7**, 294 (2013), 1207.0478.